



## Full Length Article

## Tailoring structure and surface chemistry of hollow allophane nanospheres for optimization of aggregation by facile methyl modification

Peixin Du<sup>a,b</sup>, Antoine Thill<sup>c</sup>, Peng Yuan<sup>a,b,\*</sup>, Shun Wang<sup>a,b</sup>, Dong Liu<sup>a,b</sup>, Frédéric Gobeaux<sup>c</sup>, Liangliang Deng<sup>a,b</sup>, Yaran Song<sup>a,b</sup><sup>a</sup> CAS Key Laboratory of Mineralogy and Metallogeny/Guangdong Provincial Key Laboratory of Mineral Physics and Materials, Guangzhou Institute of Geochemistry, Chinese Academy of Sciences, 511 Kehua Street, Guangzhou 510640, China<sup>b</sup> University of Chinese Academy of Sciences, 19 Yuquan Road, Beijing 100049, China<sup>c</sup> LIONS, NIMBE, CEA, CNRS, Université Paris-Saclay, CEA-Saclay, 91191 Gif sur Yvette, France

## ARTICLE INFO

## Keywords:

Allophane  
Hollow nanosphere  
Structure  
Surface chemistry  
Aggregation  
Methyl

## ABSTRACT

Allophane, an earth-abundant and easy-to-be-synthesized hollow nanospherical material, readily loses its unique pore structure via irreversible aggregation of particles upon drying, which mainly results from capillary stress in the unsaturated inner cavity. To tackle this problem, we develop a strategy for tailoring the capillary stress and thus the aggregation state of allophane by introducing methyl moieties onto the inner surface during preparation. Combined spectroscopic results verified the formation of methyl-allophane with methyl groups only on its inner surface. The presence of a reflection at approximately 33 Å in the X-ray diffraction pattern, ascribed to the interference between particles, indicated an increased structural order in methyl-allophane. The thermal analysis data revealed a decrease of the inner-surface hydrophilicity. The Brunauer-Emmett-Teller (BET) specific surface area increased from 269 to 523 m<sup>2</sup>/g after methyl modification. An aggregation model, in contrast with that of allophane, was proposed based on the microscopic and small-angle X-ray scattering results to explain these observed changes. This work exhibited that substitution of silanol by methyl on the inner surface of allophane leads to improvement of structural order by eliminating the presence of oligomeric silicates and decreases the hydrophilicity, resulting in the reduction of the capillary stress in the inner cavity and thus the inhibition of irreversible aggregation of particles during drying. The insight into the mechanisms underneath the above mentioned changes upon methyl modification unraveled in this work is helpful for addressing the common aggregation issue of other nanomaterials.

## 1. Introduction

Hollow nanospheres, classified as zero-dimension (0D) nanomaterials, are attracting increasing research attention due to their unique structures (e.g., an inner cavity for accommodating guests) and tunable inner/outer surface properties. These materials hold great promise in fields such as energy storage and conversion [1,2], drug delivery and controlled release [3], and photo- and electro-catalysis [4,5]. To date, a range of hollow spherical materials have been fabricated using noble metals (e.g., Pt), oxides (e.g., TiO<sub>2</sub>, SiO<sub>2</sub>, LiMn<sub>2</sub>O<sub>4</sub>), and carbon materials, among others [6–8]. However, most such materials have sub-micron sizes [6,9,10] and can only be obtained through complicated and expensive templating strategies [11]; solid hollow nanospheres with a diameter of a few nanometres have been rarely reported [12–14]. This largely hinders the potential applications of hollow

spherical materials in dimension-selected areas.

Allophane (1-2SiO<sub>2</sub>·Al<sub>2</sub>O<sub>3</sub>·5-6H<sub>2</sub>O, denoted Allo hereafter), a hydroxyaluminosilicate mineral that is widely distributed in soils of volcanic origin [15], is a naturally occurring hollow nanospherical material with a diameter of 3.5–5.0 nm and a wall thickness of 0.6–1.0 nm. The wall of Allo consists of a curved gibbsite-like sheet with Al<sub>2</sub>-μOH groups that are, on the inner side, substituted by orthosilicate groups. This local structure with a Si/Al molar ratio of 0.5 also occurs in imogolite (Imo, a nanotubular polymorph of Allo) and thus is called an imogolite local structure (ImoLS) [16]. Unlike Imo whose Si/Al molar ratio is 0.5, Allo has a Si/Al molar ratio of 0.5–1.0, and the excess Si is attached to the ImoLS in the form of oligomeric silicate, contributing to the low structural order of Allo. Several perforations with size of approximately 0.35 nm, formed by connection of vacancies, exist in the wall of Allo [17,18] and these perforations serve as passages for small

\* Corresponding author.

E-mail address: [yuanpeng@gig.ac.cn](mailto:yuanpeng@gig.ac.cn) (P. Yuan).<https://doi.org/10.1016/j.apsusc.2020.145453>

Received 27 November 2019; Received in revised form 5 January 2020; Accepted 17 January 2020

Available online 20 January 2020

0169-4332/ © 2020 Elsevier B.V. All rights reserved.

molecules such as H<sub>2</sub>O.

Allo originating from soils possesses a unique pore structure formed by loose stacking of particles, probably in a configuration of interleaved strings [19], which endows the Allo-rich soils with a low bulk density ( $\leq 0.85$  g/cm<sup>3</sup>), a high specific surface area (SSA, 15–90 m<sup>2</sup>/g [20]) and a large adsorption capacity towards guests [17]. However, natural Allo-rich soils are commonly multi-component, and purification procedures (e.g., removal of organic matter with H<sub>2</sub>O<sub>2</sub> and particle-size separation by sedimentation/centrifugation) are required to obtain highly pure Allo. During purification, the unique pore structure of Allo is readily destroyed via irreversible aggregation (also referred to as shrinking [21]) of particles upon drying, which largely decreases the porosity and SSA of Allo. Synthesized high-purity Allo can be produced in large amounts but readily undergoes irreversible aggregation during drying even if freeze-drying is used [22,23]. This irreversible aggregation results mainly from capillary stress in the inner cavity of unsaturated Allo [21], which represents the net interparticle stress that tends to pull one particle to another [24]. This capillary stress mainly results from the ultrasmall particle size of Allo with only short-range order in three dimensions [15,25] and the highly hydrophilic inner surface [26] due to the prevailing Si–OH therein.

In this work, tailoring the capillary stress and thus the aggregation state of Allo is achieved by introducing methyl moieties onto the inner surface during preparation. A combination of techniques, such as X-ray diffraction (XRD), X-ray absorption near-edge structure (XANES) spectroscopy, cryo-transmission electron microscopy (Cryo-TEM), small-angle X-ray scattering (SAXS), thermal analysis and N<sub>2</sub> physisorption, have been used to detect the detailed methyl-modification-induced changes of structure, surface chemistry, inner-cavity capillary stress and aggregation state in the products and the mechanisms underneath these changes. This work simply uses triethoxymethylsilane (TEMS) to replace tetraethyl orthosilicate (TEOS), the most frequently used Si source for the synthesis of Allo. The hydrolysis and condensation of the Al and methyl-bearing Si precursors resulted in the formation of nanosized fragments [16,27,28] having a general formula of (OH)<sub>3</sub>Al<sub>2</sub>O<sub>3</sub>SiOCH<sub>3</sub>, and these fragments assembled into methyl-allophane (denoted mAllo hereafter) via oriented attachment and internal reorganization when they were small enough [29]. Si–CH<sub>3</sub> groups are on the inner surface

and Al–OH groups on the outer surface of the resultant mAllo (Fig. 1a), which differs with the structure of Allo of which Si–OH groups are on the inner surface (Fig. 1b). Such a change regulates the surface properties of mAllo and effectively inhibits the irreversible aggregation of mAllo particles during drying.

## 2. Experimental section

### 2.1. Materials and methods

Orthosilicate sodium (Na<sub>4</sub>SiO<sub>4</sub>) was purchased from Alfa Aesar, USA. Aluminium chloride hexahydrate (AlCl<sub>3</sub>·6H<sub>2</sub>O), TEOS and TEMS were provided by Aldrich, USA. All chemicals and reagents used in this study were of analytical grade and used as received. Ultrapure water with a resistivity of 18.25 MΩ cm was used throughout the experiments. Methyl-imogolite (mImo) used for comparison in the SAXS analysis is the same as that previously reported [30].

The experimental procedure for synthesizing mAllo is as follows: 0.1 M AlCl<sub>3</sub> and TEMS were mixed at an initial Si/Al molar ratio of 0.75. To the resulting solution, 0.2 M NaOH was added at a rate of 1.0 mL min<sup>-1</sup> until a value of OH/Al = 2 was achieved under continuous stirring. After being stirred for another hour, the resulting dispersion was aged for one night and then heated to and maintained at 100 °C for 48 h. The dispersion was coagulated by adding diluted ammonia to approximately pH 7, centrifuged at 11000 rpm for 5 min, and dialysed for 4 days to remove the ethanol, Na<sup>+</sup> and Cl<sup>-</sup>. An aliquot of the dispersion was stored for scanning transmission electron microscopy (STEM), atomic force microscopy (AFM), cryo-TEM and SAXS characterization, and the remainder was freeze-dried. The obtained solids were labelled as mAllo. For comparison, Allo was synthesized by following the above procedure except TEOS was used instead of TEMS as a Si source.

### 2.2. Characterization techniques

XRD analysis was performed on a Bruker D8 Advance diffractometer (Manheim, Germany) with a Ni filter and Cu Kα radiation ( $\lambda = 0.154$  nm) generated at 40 kV and 40 mA. The specimens were

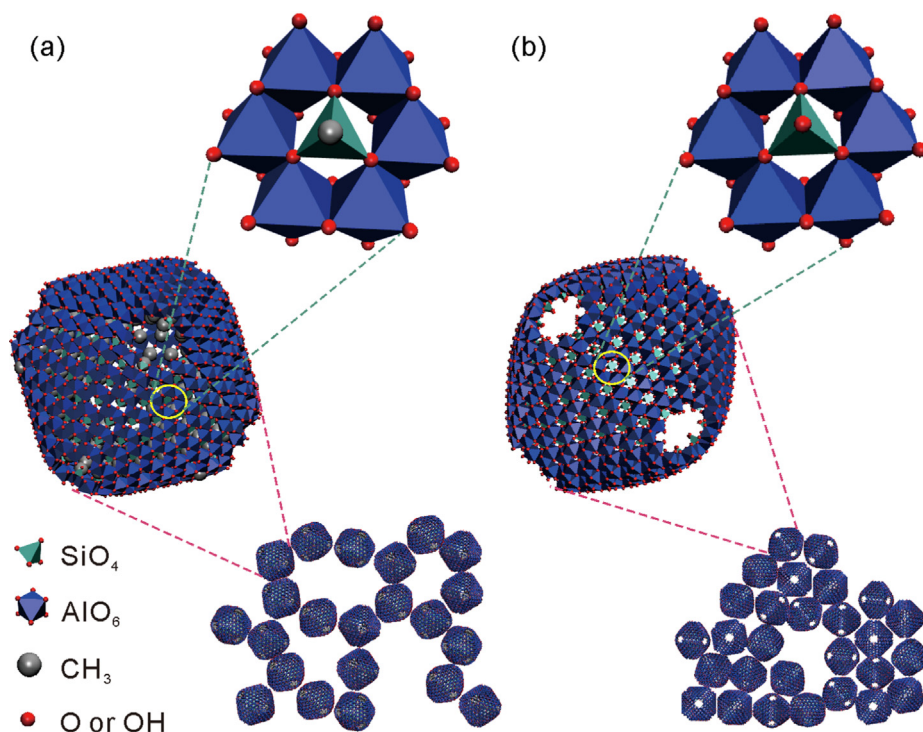


**Fig. 1.** Schematic diagram of the structures of mAllo (a) and Allo (b). Si–CH<sub>3</sub> groups on the inner surface of mAllo replace Si–OH groups (and oligomeric silicate at Si/Al molar ratios > 0.5) on the inner surface of Allo, resulting in their different aggregation states in dried powder.

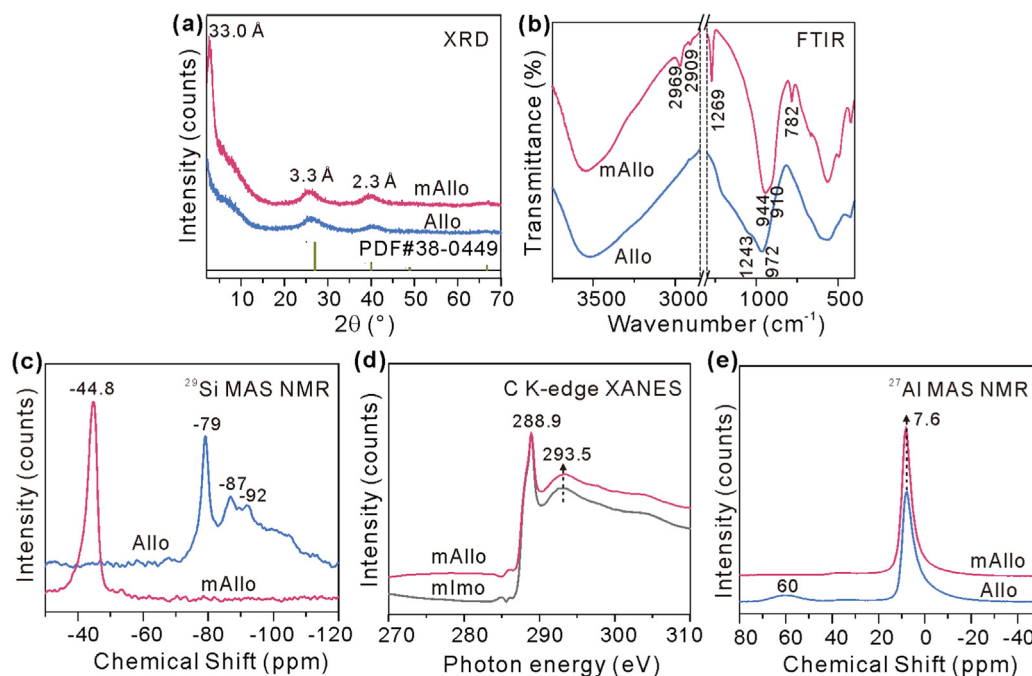


Fig. 2. XRD patterns (a), FTIR spectra (b),  $^{29}\text{Si}$  MAS NMR spectra (c), C K-edge XANES spectra (d) and  $^{27}\text{Al}$  MAS NMR spectra (e) of mAllo (a-e) and Allo (a-c, e)/mlmo (d).

scanned from  $2^\circ$  to  $70^\circ$  ( $2\theta$ ) with a step size of  $0.02^\circ$  and a measuring time of 0.8 s per step.

Fourier transform infrared (FTIR) spectra were recorded using a Bruker Vertex 70 IR spectrometer (Manheim, Germany) at room temperature. The specimens were prepared by mixing 0.9 mg of sample and 80 mg of KBr, followed by pressing the mixture into pellets. A pure KBr wafer was measured and used as the background. All of the spectra were collected over 64 scans in the range of  $4000\text{--}400\text{ cm}^{-1}$  at a resolution of  $4\text{ cm}^{-1}$ .

Solid state  $^{27}\text{Al}$  magic-angle-spinning nuclear magnetic resonance (MAS NMR) and  $^{29}\text{Si}$  MAS NMR spectra were recorded using a Bruker AVANCE III 600 spectrometer in a static magnetic field of 14.1 T at resonance frequencies of 156.4 and 119.2 MHz, respectively.  $^{27}\text{Al}$  MAS NMR spectra were recorded on a 4 mm probe by the small-flip angle technique with a pulse length of  $0.5\text{ }\mu\text{s}$  ( $< \pi/12$ ), a recycle delay of 1 s and a spinning rate of 14 kHz.  $^{29}\text{Si}$  MAS NMR spectra with high-power proton decoupling were recorded on a 4 mm probe with a spinning rate of 10 kHz, a  $\pi/4$  pulse length of  $2.6\text{ }\mu\text{s}$ , and a recycle delay of 40 s. The chemical shifts of  $^{27}\text{Al}$  and  $^{29}\text{Si}$  were referenced to 1 M  $\text{Al}(\text{NO}_3)_3$  and tetramethylsilane (TMS), respectively.

C K-edge XANES spectroscopy was recorded at the soft X-ray spectroscopy (4B7B) endstation of the Beijing Synchrotron Radiation Facility (BSRF). All the spectra were recorded at room temperature with a resolution of 0.2 eV in total electron yield (TEY) detection mode. The spectra were normalized to the incident photon flux.

The STEM images were collected on a FEI Talos F200S field-emission transmission electron microscope operating at an accelerating voltage of 200 kV. The specimens were prepared by dropping two droplets of the dispersion onto a carbon-coated copper grid.

AFM characterization was performed on a Bruker Multimode 8 scanning probe microscope with a silicon tip on a nitride lever. The ScanAsyst-air mode was used to protect the samples. To prepare the specimens, a mica sheet was cleaved (yielding a smooth negatively charged surface) and then dipped into the dispersion for 30 s. Then, two cleaning steps in water were performed to eliminate the excess materials. All of the specimens were dried in air for one week before the AFM measurements.

Cryo-TEM experiments were performed using a JEOL 2010 FEG

microscope operating at 200 kV at a low temperature ( $-180^\circ\text{C}$ ). Images were recorded with a Gatan camera. Drops of the dispersions were deposited on copper grids covered with a holey carbon film (Quantifoil R2/2) previously treated by glow discharging. The excess liquid on the grids was blotted with filter paper, and the grids were quickly immersed in liquid ethane to form a thin vitreous ice film. The whole process was conducted using a Vitrobot apparatus (FEI Company).

SAXS analysis was performed using a Xeuss 2.0 apparatus (Xenocs) under vacuum at a wavelength of  $1.542\text{ \AA}$ . The scattering vector, defined as  $q = k_d - k_i$  (the wave vectors of the incident and scattered beams) and with a modulus of  $q = 4\pi \sin \theta/\lambda$  ( $\lambda$  is the incident wavelength and  $2\theta$  is the scattering angle), ranged from  $0.03$  to  $1.2\text{ \AA}^{-1}$  and was attained with a single sample-to-detector distance. The sample-to-detector distance was calibrated with tetradecanol and the detector count was normalized by empty beam measurements. Samples were sealed in glass capillaries (diameter of 1.5 mm, wall thickness of 0.1 mm, WJM-Glas). Standard procedures were applied to obtain the differential scattering cross section per unit volume (called hereafter intensity in  $\text{cm}^{-1}$ ) as a function of  $q$  [31].

Thermogravimetric (TG) and differential scanning calorimetry (DSC) analyses were performed using a Netzsch STA 409PC instrument (Selb, Germany). Approximately 10 mg of sample was heated in a corundum crucible from 30 to  $1000^\circ\text{C}$  at a rate of  $10^\circ\text{C}/\text{min}$  in a  $\text{N}_2$  atmosphere ( $60\text{ cm}^3/\text{min}$ ).

Nitrogen adsorption-desorption isotherms were measured on a Micromeritics ASAP 2020 system (Micromeritics Co., Norcross, USA) at liquid nitrogen temperature ( $-196^\circ\text{C}$ ). Before the measurement, the samples were outgassed at  $200^\circ\text{C}$  for 12 h. The specific surface area (SSA) value was calculated using the multiple-point Brunauer-Emmett-Teller (BET) method, and the total pore volume ( $V_{\text{total}}$ ) was evaluated from the  $\text{N}_2$  uptake at a relative pressure of approximately 0.97. The  $t$ -plot method was used to calculate the microporous specific surface area ( $\text{SSA}_{\text{micro}}$ ) and the micropore volume ( $V_{\text{micro}}$ ). The pore size distribution (PSD), ranging from 0.45 to 10 nm, was analysed using non-local density functional theory (NLDFT).

### 3. Results and discussion

#### 3.1. Structural changes at molecule or local scales

The structural changes induced by methyl modification were characterized via a combination of techniques. Two reflections at 3.3 and 2.3 Å that are characteristic of ImoLS were observed in the XRD pattern of mAllo (Fig. 2a), and the overall FTIR spectrum of mAllo (Fig. 2b) resembled that of Allo, both indicating that mAllo has a structure similar to that of Allo. Bands ascribed to Si-CH<sub>3</sub> [30] (including the asymmetric and symmetric stretching vibrations at 2969 and 2909 cm<sup>-1</sup> and the bending vibration at 1269 cm<sup>-1</sup>) and to -Si-C [32] (bending vibration at 782 cm<sup>-1</sup>) appeared in the FTIR spectrum of mAllo (Fig. 2b). A new resonance at -44.8 ppm that is ascribed to T<sup>3</sup>(6Al)≡Si-CH<sub>3</sub> [33], instead of the resonance at -79 ppm that is ascribed to T<sup>3</sup>(6Al)≡Si-OH [34] and is characteristic of ImoLS [16], was observed in the <sup>29</sup>Si MAS NMR spectrum of mAllo (Fig. 2c). Moreover, the C K-edge XANES spectrum of mAllo (Fig. 2d) exhibited peaks at 288.9 and 293.5 eV, which might be attributed to the σ\*(C-H) and σ\*(C-Si) resonances, respectively. This result is almost identical to that for mImo (Fig. 2d), the structure of which has been well characterized [35], indicating the same chemical environments for C atoms (*i.e.*, T<sup>3</sup>(6Al)≡Si-CH<sub>3</sub>) in mAllo and mImo. From these results, methyl groups are assumed to be anchored to the inner surface of mAllo. The <sup>27</sup>Al MAS NMR spectrum of mAllo (Fig. 2e) was dominated by a resonance at 7.6 ppm that is ascribed to six-coordinated Al (Al<sup>VI</sup>), which is similar to the case of Allo, indicating the same chemical environments for the Al atoms (*i.e.*, a curved gibbsite-like sheet serving as the outer framework [26]) in mAllo and Allo. The above mentioned results indicate that methyl modification occurs only on the inner surface of Allo, exhibiting little effect on the outer Al-O octahedral sheet.

A shoulder band at 1243 cm<sup>-1</sup>, which appeared in the FTIR spectrum of Allo and is ascribed to the oligomeric silicate on the inner surface, was absent in the spectrum of mAllo (Fig. 2b). This is due to the presence of Si-CH<sub>3</sub> groups, which prevents the attachment of oligomeric silicate, resulting in a higher structural order in mAllo than in Allo. This assumption is further supported by the change of the band at approximately 1000 cm<sup>-1</sup> originating from the framework vibrations, of which the high-wavenumber branch was much sharper in mAllo than in Allo (Fig. 2b). Moreover, the resonance at 60 ppm in the <sup>27</sup>Al NMR spectrum of Allo, which is ascribed to four-coordinated Al (Al<sup>IV</sup>), was absent in the spectrum of mAllo (Fig. 2e). A similar change occurred for the broad resonance at approximately -90 ppm in the <sup>29</sup>Si NMR spectra (Fig. 2c), which is ascribed to a significant fraction of less ordered Si species with 0-5 next-nearest neighbour Al atoms [28]. These changes also indicate the presence of a more ordered structure in mAllo than in Allo.

#### 3.2. Changes of aggregation state and particle size

Microscopic observations showed distinct differences in aggregation behaviors between mAllo and Allo. Very small nanoparticles were observed in the STEM image of mAllo (Fig. 3a). These nanoparticles mainly occurred as interlaced strings, which is in contrast with the case of Allo where large aggregates dominated (Fig. 3b). To avoid the possible damage resulting from long-term exposure to an electron beam during STEM observation, AFM that operates under ambient conditions was used to further characterize mAllo. A similar configuration of interlaced strings was shown in the AFM images of mAllo (Fig. 3c), albeit with different specimen preparation methods for STEM and AFM. This configuration might result from the interaction between particles in the same string. This assumption was further supported by the XRD and FTIR results. On the XRD pattern of mAllo (Fig. 2a), a very-small-angle peak was observed. This new reflection is ascribed to the interference between particles arising after drying, indicating that the particles in the same string are closely linked to each other. The band at

approximately 1000 cm<sup>-1</sup> in the FTIR spectrum of Allo that arose from the Si-O stretching vibration was split into two bands at 944 and 910 cm<sup>-1</sup> in the spectrum of mAllo (Fig. 2b). This splitting phenomenon into two bands also occurred in a more pronounced way in the FTIR spectra of Imo and mImo and are characteristic of a tubular morphology [29,36]. However, the STEM and AFM results precluded the occurrence of any imogolite-like nanotubes that were produced as a byproduct (Fig. 3a, c). A possible explanation is that a moderate interparticle stress in the same string induced by capillary stress makes mAllo exhibit a similar FTIR adsorption feature as that of tubular Imo, while in the case of Allo, the presence of a strong interparticle stress prevents the formation of strings.

Cryo-TEM and SAXS have been used to characterize mAllo and Allo particles in dispersions (without potential drying artifacts). The hollow nanospherical structure of these nanoparticles, which is the most definitive feature of the Allo structure [17], was observed in the cryo-TEM images (highlighted by arrows in Fig. 3d, e). These hollow nanospheres were better dispersed (some of them were even isolated) compared to those observed in the STEM or AFM images. Unlike Allo particles that were gathered in aggregates having an average dimension of approximately 100 nm (Fig. 3e), mAllo particles were homogeneously distributed (Fig. 3d). Notably, some proto-(methyl)-imogolite-like fragments were probably present in the products (Fig. 3d, e), although they can hardly be differentiated from the nanospheres (mAllo or Allo) and quantified using cryo-TEM due to their very small sizes. The SAXS measurements of both Allo and mAllo revealed an increase of the intensity at the lowest scattering angles (Fig. 3g). The smooth increase of the intensity is characteristic of disordered (fractal) aggregates in dispersions. This is in good agreement with the cryo-TEM observations where both samples displayed aggregates (Fig. 3d, e). From these above microscopic and SAXS results, it is found that hollow nanospheres prevail in both Allo and mAllo and that methyl modification induces changes in the arrangements of these nanospheres in both liquid and dried powder.

Thanks to the high z-axis resolution of AFM, an average particle size of 3-5 nm (with appropriately 3 nm being dominant) of the mAllo particles was recorded (Fig. 3f). This average size agrees with the previously reported values of Allo obtained by electron microscopy [17]. This result indicates that the overall particle size of Allo remained in the same range upon methyl modification. Similar SAXS curves with weak oscillations were observed for both samples (Fig. 3g). The positions of these oscillations enable to access the average characteristic dimensions of mAllo and Allo through comparison with the oscillation positions of modeled core-shell particles [30,36]. The dimensions that yield oscillations at the closest positions indicate an inner/external diameter of 3.6/4.8 nm for mAllo and 2.4/3.6 nm for Allo (Fig. 3g). Notably, in addition to mAllo particles with sizes of 3-5 nm, a few of particles with z-scans of less than 1 nm were observed (Fig. 3f). It is likely that these particles are proto-methyl-imogolite-like fragments that adsorb flat on mica sheets, as previously reported [16]. Despite not being fully quantitative, the proportion of the particles with different sizes, summarized from the repeated section analyses of the AFM images, indicates that hollow nanosphere is the dominating morphology of the nanoparticles.

#### 3.3. Changes of surface hydrophilicity

These structural changes result in modification of the inner-surface hydrophilicity of the products. As exhibited in the TG curves (Fig. 4), for the mass loss below 150 °C, which is mainly attributed to the desorption of physisorbed water [26], a lower temperature was required for mAllo than for Allo to lose the same mass. The corresponding endothermic peak in the DSC curves also occurred at a lower temperature for mAllo than for Allo (Fig. 4). These results indicate that the physisorbed water in mAllo is removable at a lower temperature than that in Allo; that is, the inner surface of mAllo is less hydrophilic than that of

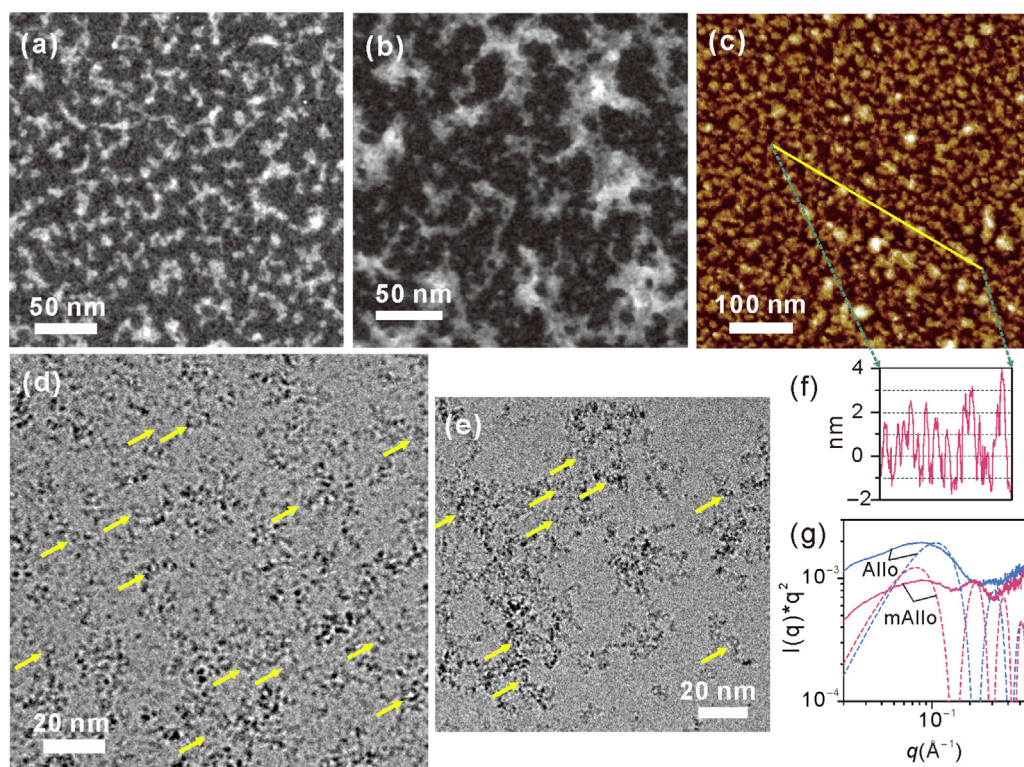


**Fig. 3.** STEM images of mAllo (a) and Allo (b), AFM image of mAllo (c) and cryo-TEM images of mAllo (d) and Allo (e). (f) Cross-section profile of the yellow line in (c), showing average particle sizes of 3–5 nm. (g) SAXS curves of mAllo and Allo. Arrows in (d) and (e) highlight the presence of hollow nanospheres. The dash line in (g) represents the expected scattering curves for monodispersed core-shell spheres with external (inner) diameters of 4.8 (3.6) and 3.6 (2.4) nm, respectively. (For interpretation of the references to colour in this figure legend, the reader is referred to the web version of this article.)

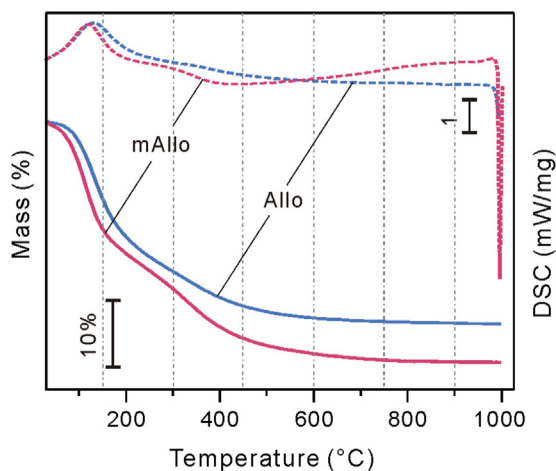


**Fig. 4.** TG-DSC curves of mAllo and Allo.

Allo.

### 3.4. Changes of porosity and specific surface area

According to the International Union of Pure and Applied Chemistry (IUPAC) recommendation [37], the  $N_2$  physisorption isotherms of mAllo and Allo are characterized as type I (Fig. 5a), indicating that both materials are dominated by micropores. The SSA and  $V_{total}$  of mAllo (523  $m^2/g$  and 0.2273  $cm^3/g$ ) were much higher than those of Allo (269  $m^2/g$  and 0.1222  $cm^3/g$ ) (Table 1). As discussed above, methyl modification results in limited changes in the particle sizes and outer structural framework of Allo. The high SSA and porosity of mAllo arise from the configuration of interlaced strings. In addition, the PSD curves derived using a NLDFT method (Fig. 5b) exhibited a distinct difference. Specifically, micropores with wide-ranging diameters were observed in Allo, while pores with diameters of approximately 2 nm dominated in mAllo. This difference might be because the pores in Allo originated

from cavities between aggregates formed by the irreversible aggregation of particles, while the pores in mAllo arose from the network formed by the interleaving of strings of particles (as schematically shown in Fig. 1).

### 3.5. Mechanisms underneath the above mentioned changes

As discussed above, the introduction of Si-CH<sub>3</sub> to the inner surface of mAllo makes this surface less hydrophilic than that of Allo. The weakened surface hydrophilicity decreases the capillary stress in the inner cavity of mAllo and thus inhibits the irreversible aggregation of particles during drying, resulting in higher SSA and porosity values. On the other hand, the absence of Si-OH on the inner surface of mAllo prevents the formation of oligomeric silicate therein and thus increases the structural order and total pore volume of this material. Notably, the simultaneous absence of oligomeric silicate and Al<sup>IV</sup> in mAllo might provide insight into the probable location of Al<sup>IV</sup> in the Allo structure; i.e., Al<sup>IV</sup> might be mainly located in oligomeric silicate by substituting Si on the inner surface, which sheds light on the long-standing question of whether Al<sup>IV</sup> is located around the perforations on the wall [38] or in the oligomeric silicate upon substituting Si atoms [39] in the Allo structure. This assumption is further supported by the fact that scarcely any Al<sup>IV</sup> occurs in Imo consisting of only ImoS [28].

## 4. Conclusion

Tailoring the structure and surface chemistry and thus the aggregation state of hollow Allo nanospheres has been achieved by a simple strategy of methyl modification. The as-obtained mAllo is a novel hollow nanospherical material with a higher structural order, a much less hydrophilic inner surface and a larger porosity and SSA than Allo, which allow its promising applications in a variety of fields such as selective gas adsorption. This facile inner-surface methyl-modification method and the basic knowledge on the mechanisms underneath the changes of the structure, surface chemistry, inner-cavity capillary stress and aggregation state of Allo nanospheres reported in this work is of

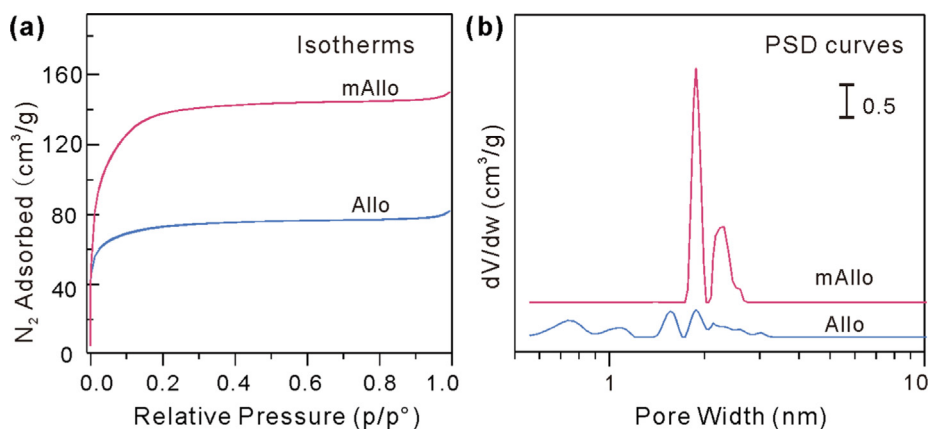


Fig. 5.  $N_2$  adsorption/desorption isotherms (a) and PSD curves (b) of mAllo and Allo.

**Table 1**

Textural data of mAllo and Allo obtained from  $N_2$  adsorption analysis.

	SSA ( $m^2/g$ )	SSA <sub>micro</sub> ( $m^2/g$ )	$V_{total}$ ( $cm^3/g$ )	$V_{micro}$ ( $cm^3/g$ )
Allo	269.5	267.2	0.1222	0.1156
mAllo	523.1	519.6	0.2273	0.2191

great significance for dealing with the common aggregation issue of other nanomaterials.

#### CRediT authorship contribution statement

**P. Du:** Conceptualization, Writing - original draft, Investigation, Visualization, Validation. **A. Thill:** Conceptualization, Writing - original draft, Investigation, Visualization, Validation. **P. Yuan:** Conceptualization, Writing - original draft, Funding acquisition, Project administration, Investigation, Visualization, Validation. **S. Wang:** Investigation, Visualization, Validation. **D. Liu:** Investigation, Visualization, Validation. **F. Gobeaux:** Methodology, Investigation, Visualization, Validation. **L. Deng:** Investigation, Visualization, Validation. **Y. Song:** Investigation, Visualization, Validation.

#### Declaration of Competing Interest

The authors declare that they have no known competing financial interests or personal relationships that could have appeared to influence the work reported in this paper.

#### Acknowledgements

This work is supported by the Science and Technology Planning Project of Guangdong Province, China (2017B020237003), the National Natural Science Foundation of China (41672042 and 41972045), Youth Innovation Promotion Association CAS for the excellent members (2016-81-01), the China Postdoctoral Science Foundation (2018M640831) and the Open Funds of the Beijing Synchrotron Radiation Facility (2017-BEPC-PT-001065). Cryo-TEM observations were made, thanks to "Investissements d'Avenir" LabEx PALM (ANR-10-LABX-0039-PALM). This is a contribution (No. IS-2805) from GIGCAS.

#### References

- [1] M. Sasidharan, K. Nakashima, N. Gunawardhana, T. Yokoi, M. Inoue, S.-I. Yusa, M. Yoshio, T. Tatsumi, Novel titania hollow nanospheres of size  $28 \pm 1$  nm using soft-templates and their application for lithium-ion rechargeable batteries, *Chem. Commun.* 47 (2011) 6921–6923.
- [2] M.Q. Zhu, S.M. Li, J.H. Liu, B. Li, Promoting polysulfide conversion by  $V_2O_5$  hollow sphere for enhanced lithium-sulfur battery, *Appl. Surf. Sci.* 473 (2019) 1002–1008.
- [3] Y. Hu, Y. Ding, D. Ding, M. Sun, L. Zhang, X. Jiang, C. Yang, Hollow chitosan/poly (acrylic acid) nanospheres as drug carriers, *Biomacromolecules* 8 (2007) 1069–1076.
- [4] H.P. Liang, H.M. Zhang, J.S. Hu, Y.G. Guo, L.J. Wan, C.L. Bai, Pt hollow nanospheres: facile synthesis and enhanced electrocatalysts, *Angew. Chem. Int. Edit.* 43 (2004) 1540–1543.
- [5] M. Tian, X.L. Cui, C.X. Dong, Z.P. Dong, Palladium nanoparticles dispersed on the hollow aluminosilicate microsphere@hierarchical gamma-ALOOH as an excellent catalyst for the hydrogenation of nitroarenes under ambient conditions, *Appl. Surf. Sci.* 390 (2016) 100–106.
- [6] F. Xu, Z. Tang, S. Huang, L. Chen, Y. Liang, W. Mai, H. Zhong, R. Fu, D. Wu, Facile synthesis of ultrahigh-surface-area hollow carbon nanospheres for enhanced adsorption and energy storage, *Nat. Commun.* 6 (2015) 7221.
- [7] W.J. Wu, W.T. Qi, Y.F. Zhao, X. Tang, Y.F. Qiu, D.W. Su, H.B. Fan, G.X. Wang, Hollow  $CeO_2$  spheres conformally coated with graphitic carbon for high-performance supercapacitor electrodes, *Appl. Surf. Sci.* 463 (2019) 244–252.
- [8] A.E. Awadallah, W. Ahmed, M.R.N. El-Din, A.A. Aboul-Enein, Novel aluminosilicate hollow sphere as a catalyst support for methane decomposition to  $CO_2$ -free hydrogen production, *Appl. Surf. Sci.* 287 (2013) 415–422.
- [9] G. Zheng, S.W. Lee, Z. Liang, H.-W. Lee, K. Yan, H. Yao, H. Wang, W. Li, S. Chu, Y. Cui, Interconnected hollow carbon nanospheres for stable lithium metal anodes, *Nat. Nanotechnol.* 9 (2014) 618–623.
- [10] Z. Zhou, J. Gu, X. Qiao, H. Wu, H. Fu, L. Wang, H. Li, L. Ma, Double protected lanthanide fluorescence core@shell colloidal hybrid for the selective and sensitive detection of  $ClO^-$ , *Sens. Actuators B: Chem.* 282 (2019) 437–442.
- [11] X.W. Lou, L.A. Archer, Z. Yang, Hollow micro-/nanostructures: synthesis and applications, *Adv. Mater.* 20 (2008) 3987–4019.
- [12] B.H. Bac, Y. Song, M.H. Kim, Y.-B. Lee, I.M. Kang, Single-walled hollow nanospheres assembled from the aluminogermanate precursors, *Chem. Commun.* (2009) 5740–5742.
- [13] M.B. Tahir, G. Nabi, N.R. Khalid, W.S. Khan, Synthesis of nanostructured based  $WO_3$  materials for photocatalytic applications, *J. Inorg. Organomet. P.* 28 (2018) 777–782.
- [14] Y. Wu, H. Wang, W. Tu, Y. Liu, Y.Z. Tan, X. Yuan, J.W. Chew, Quasi-polymeric construction of stable perovskite-type  $LaFeO_3/g-C_3N_4$  heterostructured photocatalyst for improved Z-scheme photocatalytic activity via solid p-n heterojunction interfacial effect, *J. Hazard. Mater.* 347 (2018) 412–422.
- [15] C. Levard, E. Doelsch, I. Basile-Doelsch, Z. Abidin, H. Mische, A. Masion, J. Rose, D. Borschneck, J.Y. Bottero, Structure and distribution of allophanes, imogolite and proto-imogolite in volcanic soils, *Geoderma* 183 (2012) 100–108.
- [16] P. Du, P. Yuan, A. Thill, F. Annabi-Bergaya, D. Liu, S. Wang, Insights into the formation mechanism of imogolite from a full-range observation of its sol-gel growth, *Appl. Clay Sci.* 150 (2017) 115–124.
- [17] R. Parfitt, Allophane and imogolite: role in soil biogeochemical processes, *Clay Miner.* 44 (2009) 135–155.
- [18] B. Creton, D. Bougeard, K.S. Smirnov, J. Guilmont, O. Poncelet, Structural model and computer modeling study of allophane, *J. Phys. Chem. C* 112 (2008) 358–364.
- [19] Y. Adachi, J. Karube, Application of a scaling law to the analysis of allophane aggregates, *Colloid Surface A* 151 (1999) 43–47.
- [20] S. Filimonova, S. Kaufhold, F.E. Wagner, W. Häusler, I. Kögel-Knabner, The role of allophane nano-structure and Fe oxide speciation for hosting soil organic matter in an allophanic Andosol, *Geochim. Cosmochim. Ac.* 180 (2016) 284–302.
- [21] T. Woignier, J. Primera, L. Duffours, P. Dieudonné, A. Raada, Preservation of the allophanic soils structure by supercritical drying, *Micropor. Mesopor. Mater.* 109 (2008) 370–375.
- [22] F. Ohashi, S.-I. Wada, M. Suzuki, M. Maeda, S. Tomura, Synthetic allophane from high-concentration solutions: nanoengineering of the porous solid, *Clay Miner.* 37 (2002) 451–456.
- [23] J. Castello, J.J. Gaumet, J.F. Muller, S. Derousseaux, J. Guilmont, O. Poncelet, Laser ablation of aluminosilicates: Comparison between allophane and mixed alumina/silicas by Fourier Transform-Ion Cyclotron Resonance-Mass Spectrometry, *Appl. Surf. Sci.* 253 (2007) 7773–7778.

- [24] W.J. Likos, N. Lu, Hysteresis of capillary stress in unsaturated granular soil, *J Eng Mech-Asce* 130 (2004) 646–655.
- [25] D. Wang, A. Fernandez-Martinez, Order from disorder, *Science* 337 (2012) 812–813.
- [26] P. Du, P. Yuan, D. Liu, S. Wang, H. Song, H. Guo, Calcination-induced changes in structure, morphology, and porosity of allophane, *Appl. Clay Sci.* 158 (2018) 211–218.
- [27] V. Farmer, A. Fraser, J. Tait, Synthesis of imogolite: a tubular aluminum silicate polymer, *J. Chem. Soc., Chem. Commun.* (1977) 462–463.
- [28] G.I. Yucelen, R.P. Choudhury, A. Vyalikh, U. Scheler, H.W. Beckham, S. Nair, Formation of single-walled aluminosilicate nanotubes from molecular precursors and curved nanoscale intermediates, *J. Am. Chem. Soc.* 133 (2011) 5397–5412.
- [29] A. Thill, P. Picot, L. Belloni, A mechanism for the sphere/tube shape transition of nanoparticles with an imogolite local structure (imogolite and allophane), *Appl. Clay Sci.* 141 (2017) 308–315.
- [30] Y. Liao, P. Picot, J.-B. Brubach, P. Roy, S. Le Caër, A. Thill, Self-supporting thin films of imogolite and imogolite-like nanotubes for infrared spectroscopy, *Appl. Clay Sci.* 164 (2017) 58–67.
- [31] P. Lindner, T. Zemb, Neutrons, X-rays and Light: Scattering Methods Applied to Soft Condensed Matter, Elsevier, 2002.
- [32] M. Boyer, E. Paineau, M. Bacia-Verloop, A. Thill, Aqueous dispersion state of amphiphilic hybrid aluminosilicate nanotubes, *Appl. Clay Sci.* 96 (2014) 45–49.
- [33] D.-Y. Kang, N.A. Brunelli, G.I. Yucelen, A. Venkatasubramanian, J. Zang, J. Leisen, P.J. Hesketh, C.W. Jones, S. Nair, Direct synthesis of single-walled aminoaluminosilicate nanotubes with enhanced molecular adsorption selectivity, *Nat. Commun.* 5 (2014) 3342.
- [34] P.F. Barron, M.A. Wilson, A.S. Campbell, R.L. Frost, Detection of imogolite in soils using solid-state Si-29 NMR, *Nature* 299 (1982) 616–618.
- [35] I. Bottero, B. Bonelli, S.E. Ashbrook, P.A. Wright, W.Z. Zhou, M. Tagliabue, M. Armandi, E. Garrone, Synthesis and characterization of hybrid organic/inorganic nanotubes of the imogolite type and their behaviour towards methane adsorption, *Phys. Chem. Chem. Phys.* 13 (2011) 744–750.
- [36] M.S. Amara, S. Rouzière, E. Paineau, M. Bacia-Verloop, A. Thill, P. Launois, Hexagonalization of aluminogermanate imogolite nanotubes organized into closed-packed bundles, *J. Phys. Chem. C* 118 (2014) 9299–9306.
- [37] M. Thommes, K. Kaneko, A.V. Neimark, J.P. Olivier, F. Rodriguez-Reinoso, J. Rouquerol, K.S. Sing, Physisorption of gases, with special reference to the evaluation of surface area and pore size distribution (IUPAC Technical Report), *Pure Appl. Chem.* 87 (2015) 1051–1069.
- [38] H. Shimizu, T. Watanabe, T. Henmi, A. Masuda, H. Saito, Studies on allophane and imogolite by high-resolution solid-state <sup>29</sup>Si- and <sup>27</sup>Al-NMR and ESR, *Geochem. J.* 22 (1988) 23–31.
- [39] B. Goodman, J. Russell, B. Montez, E. Oldfield, R. Kirkpatrick, Structural studies of imogolite and allophanes by aluminum-27 and silicon-29 nuclear magnetic resonance spectroscopy, *Phys. Chem. Miner.* 12 (1985) 342–346.